AIAA JOURNAL
Vol. 50, No. 9, September 2012

Reynolds-Averaged Navier–Stokes Computations of Synthetic Jet Flows Using Deforming Meshes

Ilyong Yoo* and Seungsoo Lee†
Inha University, Incheon 402-751, Republic of Korea

DOI: 10.2514/1.J051539

Realistic computations of flows induced by synthetic jets in multiple flow conditions are studied with an unsteady preconditioned Reynolds-averaged Navier–Stokes solver with deforming meshes. Deforming meshes suitable for structured grid systems are used to simulate the motion of diaphragms driven at a given frequency. With deforming meshes, a boundary-condition model is not necessary for synthetic jet calculations. To obtain time-accurate solutions with a grid system under deformation, the geometric conservation law is employed. Numerical calculations of three cases of the Langley Research Center Workshop Computational Fluid Dynamics Validation of Synthetic Jets and Turbulent Separation Control workshop are carried out, and the computational results are compared with the experimental data. The results indicate the effectiveness of the current method in synthetic jet flow computations.

Nomenclature

F	=	inviscid flux vector
f	=	frequency
F_v	=	viscous flux vector
J_n	=	nth-order Bessel function of the first kind
k	=	normal velocity component relative to moving computational cell boundary
M	=	Mach number
p	=	gauge pressure
Q_p	=	primitive flow variable vector
S	=	source vector
V	=	control volume
W	=	conservative flow variable
Γ	=	preconditioning matrix
δV	=	outer surface of a control volume
μ_m	=	molecular viscosity
μ_t	=	turbulent viscosity
$\boldsymbol{\xi}$	=	grid velocity
τ_{ij}	=	shear stress tensor
ϕ, θ	=	time-integration method identifier
ψ	=	net volume swept by a moving computational cell
Ω_i	=	total energy flux vector

I. Introduction

FOR years, many studies in the aerospace field have focused on the advantages of active flow control. Flow control to delay flow separation, to increase lift, or to enhance thrust, however, is obtainable only with a cost increase and a weight increase. For instance, traditional boundary-layer control through steady suction or blowing is effective in increasing lift-to-drag ratios of airfoils and has been implemented in production aircraft such as the Lockheed F-104. However, successful implementation of steady suction or blowing control is limited due to the complexity and weight of the flow-control systems. In recent years, active flow control using synthetic jets has received wide attention due to its superiority to other flow-control devices; its merits include low cost, compact design, and lack of external apparatus. Synthetic jets synthesize incoming and outgoing air through an orifice via slots mounted on wings and controlled by actuators, which means that there is no need of any other mass source. The actuation frequency and waveform of the synthetic jets can usually be customized for a particular flow configuration. Many researchers have studied and tested these synthetic jets in a variety of applications. The effectiveness of a zero-net-mass flux device in flow control has been proven experimentally and numerically.

Most of the early investigations on synthetic jets relied on empirical approaches because of the lack of observations and physical explanations for the flowfield induced by the synthetic jets. Among those studies, Smith and Glezer [1] investigated the characteristics of synthetic jets by synthesizing a plain turbulent jet with a flexible diaphragm in a sealed cavity. They showed experimentally how the synthetic jets developed through the interactions of a series of counter-rotating vortex pairs that formed at the edge of an orifice. They also demonstrated jet vectoring with the combination of a primary conventional rectangular air jet and a synthetic jet [2]. They concluded that the subsequent formation of a low-pressure region between the jets resulted in deflection of the primary jet toward the actuator jet without an extended control surface, and that the formation of the low-pressure region was balanced by a force on the primary jet conduit. Chen et al. [3] demonstrated that synthetic jet actuators could enhance mixing in a gas turbine combustor. They used two streams of different temperatures to simulate mixing in a dilution zone. The temperature distribution downstream of the synthetic jet was measured to determine the effectiveness of mixing. Their experiments showed that synthetic jet devices could improve mixing in a turbine engine combustor. Smith et al. [4] showed that a synthetic jet located near the leading edge of a thick airfoil could make a separated shear layer reattach on the upper surface of the airfoil at stall. When compared with the pressure distribution over the airfoil without flow control, the lift coefficient more than doubled while the drag coefficient was reduced by a factor of two. They also investigated the effect of jet location and amplitude on the separation efficiency. It was demonstrated that as the position of the jet approached the separation point in the stalled flow, the jet strength required to make the separated flow attach decreased by more than an order of magnitude.

With the advances in computational fluid dynamics (CFD) and computer technology, numerical simulations of unsteady flows around complex geometries have become possible. The results of these computations have been found to agree well with experimental data. However, most of the numerical studies were done without the benefit of experimental research. Recently, numerical research

Presented as Paper 2011-942, at the 49th AIAA Aerospace Sciences Meeting including the New Horizons Forum and Aerospace Exposition, Orlando, Florida, 4–7 January 2011; received 2 August 2011; revision received 27 December 2011; accepted for publication 10 February 2012.

*Ph.D. Candidate, Department of Aerospace Engineering, 253 Yonghyun-dong, Nam-gu. Student Member AIAA.

†Professor, Department of Aerospace Engineering, 253 Yonghyun-dong, Nam-gu. Senior Member AIAA.

groups and experimental research groups have recognized the need for mutual exchange of opinions as well as of results. One of the efforts was the Langley Research Center Workshop CFD Validation of Synthetic Jets and Turbulent Separation Control (CFDVAL2004) workshop, which was held in Williamsburg, Virginia, in 2004. Well-documented experiments on synthetic jets over three types of external flow provide a database that can be used for the development of CFD techniques capable of simulating separation and control of flows. This database provides challenging test cases for CFD validation due to arbitrarily curved geometry, unsteady separation and reattachment, and a Reynolds-number separation bubble. The experimental data and the workshop results were made available on a public website to widen the community of researchers interested in active flow control using synthetic jets.

Rumsey et al. [5,6] collected the numerical results and published two excellent review papers in 2004 and 2008. Yamaleev and Carpenter [7] showed that three-dimensional synthetic jet flow problems could be solved with the quasi-one-dimensional Euler equations. Based on their observations, they suggested that this model could be used for two-dimensional or three-dimensional computations for computational efficiency. Similarly, Vatsa and Turkel [8] and Park et al. [9] performed two-dimensional unsteady Reynolds-averaged Navier–Stokes (URANS) simulations of synthetic jets with the boundary models. These three previous studies were conducted with some geometric approximation of the actuators and with boundary-condition models that mimicked synthetic jet flow. Cui and Agarwal [10] performed both two-dimensional and three-dimensional URANS simulations for synthetic jets including the cavity of case 1. Also, they applied the same methodology to case 2 of the CFDVAL2004 workshop, which is three-dimensional [11]. In addition, Balakumar [12] analyzed case 3 with the Reynolds-averaged Navier–Stokes (RANS) equations and a boundary-condition model. However, these studies adopted boundary-condition models to simulate the velocity profile generated by the oscillating motion of the diaphragms. Although the boundary-condition models have been successfully used to compute synthetic jet flows, the methods rely on an approximation of the boundary conditions that determine the flows. Because of the inability to accurately account for the geometry of the actuator, those computations cannot include viscous effects associated with the flow through the orifice, or the near-field flow physics caused by the interaction of the external boundary layer and the actuator. Yoo et al. [13] presented a two-dimensional computation of case 1 of the CFDVAL2004 workshop using an exact jet model. The exact model did not employ any boundary-condition model. Instead, the flow induced by the movement of the diaphragm was computed directly with a deforming mesh inside the synthetic jet. The geometry conservation law was used to ensure the conservation of the freestream with the deforming grid.

The objective of our work is to show the ability to simulate synthetic jet flows, including the full three-dimensional shape of the actuator, using the exact jet model. Flows induced by synthetic jets into quiescent air, into a turbulent crossflow boundary layer, and into a turbulent separation flow are investigated in this study. To simulate the flows inside the cavity, a transfinite interpolation (TFI) method with a linear blending function is adopted to automatically generate grids that deform according to the oscillation of the diaphragm. Simultaneously, the volume of the cell is evaluated so that it satisfies the geometric conservation. For case 1 of the CFDVAL2004 workshop, the motion of the circular diaphragm is modeled as the solution of a two-dimensional wave equation in polar coordinates. For cases 2 and 3, the motion is modeled by combining the rigid-body motion and the elastic motion. Time-dependent solutions to the evolution of a synthetic jet are obtained by solving the time-dependent compressible RANS equations with a two-equation turbulence model. Because the range of the Mach number extends from the incompressible to the compressible regimes, the preconditioning method of Weiss and Smith [14] is used to perform an accurate simulation. Menter's k-ω shear stress transport (SST) turbulence model [15] is used to account for the turbulent nature of the flows. Detailed comparisons of the phase-averaged results and the time-averaged results of the velocity components and the pressure coefficient are presented. The effects of the exact model on the synthetic jet simulations are discussed.

II. Governing Equations and Numerical Methods

A. Preconditioned Reynolds-Averaged Navier–Stokes Equations

The unsteady RANS equations are chosen as governing equations for the synthetic jet problems. As mentioned in the introduction, the preconditioning method is applied to take account of the low Mach number region. The integral form of the governing equations over a moving control volume, V, including a fictitious time term for dual time-stepping method, is given by

$$\Gamma\frac{\mathrm{d}}{\mathrm{d}\tau}\int_V Q_p\,\mathrm{d}V+\frac{\mathrm{d}}{\mathrm{d}t}\int_V W\,\mathrm{d}V+\int_{\delta V}\mathbf{F}\cdot\hat{n}\,\mathrm{d}S=\int_{\delta V}\mathbf{F}_v\cdot\hat{n}\,\mathrm{d}S+\int_V S\,\mathrm{d}V \tag{1}$$

where the conservative solution vector, W, the primitive solution vector, Q_p, the inviscid flux vector, F, the viscous flux vector, F_v, and the source vector, S, are defined by

$$W=\begin{bmatrix}\rho\\ \rho u\\ \rho v\\ \rho w\\ e\\ \rho K\\ \rho\omega\end{bmatrix},\qquad Q_p=\begin{bmatrix}p\\ u\\ v\\ w\\ T\\ K\\ \omega\end{bmatrix},$$

$$F=(\mathbf{F}-W\boldsymbol{\xi})\cdot\hat{n}=\begin{bmatrix}\rho k\\ \rho ku+pn_x\\ \rho kv+pn_y\\ \rho kw+pn_z\\ (e+p)k+p\xi_t\\ \rho kK\\ \rho k\omega\end{bmatrix},\qquad F_v=\mathbf{F}_v\cdot\hat{n}=\begin{bmatrix}0\\ n_x\tau_{xx}+n_y\tau_{yx}+n_z\tau_{zx}\\ n_x\tau_{xy}+n_y\tau_{yy}+n_z\tau_{zy}\\ n_x\tau_{xz}+n_y\tau_{yz}+n_z\tau_{zz}\\ n_x\Omega_x+n_y\Omega_y+n_z\Omega_z\\ (\mu_m+\sigma_K\mu_t)\hat{n}\cdot\nabla K\\ (\mu_m+\sigma_\omega\mu_t)\hat{n}\cdot\nabla\omega\end{bmatrix},\qquad S=\begin{bmatrix}0\\ 0\\ 0\\ 0\\ 0\\ S_K\\ S_\omega\end{bmatrix} \tag{2}$$

Here, k and ξ_t are the relative velocity component normal to the surfaces of the control volume, and the grid velocity component normal to the surfaces, respectively. They are defined by the following:

$$k=n_xu+n_yv+n_zw-\xi_t \tag{3}$$

$$\xi_t=\xi_xn_x+\xi_yn_y+\xi_zn_z \tag{4}$$

In addition, σ_K and σ_ω are the turbulent model constants. As stated earlier, Menter's K-ω SST turbulence model is used in this study [15]. The matrix, Γ, premultiplied by the time derivative term in Eq. (1), is the preconditioning matrix that is used to reduce the condition number of the system for low Mach number flows. We choose the matrix of Weiss and Smith [14] to reduce the stiffness of the governing equations and to enhance the convergence of the iterative solutions.

B. Numerical Methods

Upon integrating Eq. (1) over a hexahedron, we have

$$\Gamma\frac{\partial Q_p}{\partial\tau}+\frac{\partial W}{\partial t}=-R \tag{5}$$

where the residual vector is given by

$$R = \frac{1}{V}\left(\sum F\Delta S - \sum F_v \Delta S - VS\right) \tag{6}$$

where ΔS is the surface of the hexahedron. The inviscid flux in Eq. (6) is replaced by Roe's numerical flux [16] for numerical stability:

$$\hat{F}_{i+1/2} = \frac{1}{2}[F(Q_p^R) + F(Q_p^L) - \Gamma|A_\Gamma|(Q_p^R - Q_p^L)] \tag{7}$$

where A_Γ is the preconditioned Jacobian matrix of the flux vector F. MUSCL extrapolation [17] for Q_p^R and Q_p^L is used for higher spatial accuracy. Van Albada's limiter is adopted to maintain the total variation diminishing property near the sharp solution gradient region. The gradient theorem is used to compute the derivatives of flow variables, which are needed to compute viscous terms.

Upon applying the Beam and Warming method [18] and the dual time-stepping method [19] to Eq. (5), the discretization equations are found to be

$$\left(1 + \frac{\phi}{2}\right)\frac{\Delta(\overline{VW})}{\Delta t} - \frac{\phi}{2}\frac{\Delta(VW)^{n+1}}{\Delta t} + \Gamma\frac{\Delta(VQ_p)^l}{\Delta\tau} + \theta R^{l+1} + (1-\theta)R^n = 0 \tag{8}$$

where l is the iteration level of the dual time stepping and n is the physical time level. The time-integration method identifiers are ϕ and θ. Equation (8) becomes a second-order method with $\phi = 1$, whereas it becomes a first-order method with $\phi = 0$. The Euler implicit method corresponds to $\theta = 1$, whereas the trapezoidal method corresponds to $\theta = 1/2$. In this paper, $\phi = 1$ and $\theta = 1$ are used, which yields second-order temporal accuracy. Also, the corrections are defined by

$$\begin{aligned}
\Delta(\overline{VW}) &= V^{n+1}W^{l+1} - (VW)^n,\\
\Delta(VW)^{n-1} &= (VW)^n - (VW)^{n-1},\\
\Delta(VW)^l &= V^{n+1}(W^l - W^{l-1})
\end{aligned} \tag{9}$$

The approximated factorization-alternate direction implicit (AF-ADI) method [20] along the fictitious time is applied to Eq. (8); that is,

$$\left[D + \theta\frac{\Delta\tau}{V}A\right]D^{-1}\left[D + \theta\frac{\Delta\tau}{V}B\right]D^{-1}\left[D + \theta\frac{\Delta\tau}{V}C\right]\Delta Q_p = -\Delta\tau\tilde{R} \tag{10}$$

In Eq. (10), A, B, C, and D are factored operators. The detailed expression for the operators can be found in [21]. The unsteady residual vector $\tilde{R}$ is given by

$$\tilde{R} = \frac{1}{V^{n+1}}\left[\left(1 + \frac{\phi}{2}\right)\frac{V^{n+1}Q^l - (VQ)^n}{\Delta t} - \frac{\phi}{2}\frac{(VQ)^n - (VQ)^{n-1}}{\Delta t} + \theta R^l + (1-\theta)R^n\right] \tag{11}$$

The dual time-stepping method can reduce the factorization error as well as the linearization error associated with the AF-ADI method. Furthermore, the time lag error due to the explicit boundary-condition method can be minimized.

Equation (10) is solved with a loosely coupled method. The loosely coupled method solves the Navier–Stokes equations first with the turbulent viscosity fixed. Subsequently, the turbulence model equations are solved with the mean flow quantities fixed. One of the merits of using the loosely coupled method is the relative simplicity of implementing the turbulence model equations into the Navier–Stokes equations. According to Lee and Choi's work [21], differences in the stability characteristics of a strongly coupled method and those of a loosely coupled method are negligible.

III. Deforming Mesh Generation

It is necessary to automatically generate the grid inside the cavity of the synthetic jet in order to successfully compute flows induced by the moving diaphragm. In this paper, a TFI method [22] is adopted. TFI has advantages over other grid-generation methods. It is comparably fast to run, easy to implement, and suitable for structured meshes. The linear blending function with the arc-length control function [23] is chosen for computational efficiency.

IV. Geometric Conservation Law

If only the geometric consideration for the evaluation of the volume of a computational cell is made when the grid is deforming, the numerical solutions may not conserve a freestream. The geometric conservation law, therefore, must be applied to ensure that a uniform flow is an exact solution to the discretized Navier–Stokes equations with the grid deforming [24]. Upon plugging the uniform flow condition, $Q = \text{const}$, into the Navier–Stokes equations, the integral form of the geometric conservation law is obtained:

$$\frac{\partial}{\partial t}\int_V \mathrm{d}V - \int_{\delta V} \boldsymbol{\xi}\cdot\hat{n}\,\mathrm{d}S = 0 \tag{12}$$

By applying the same discretization as that of the Navier–Stokes equations, we obtain the discretized form of the geometric conservation law:

$$V^{n+1} = V^n + \frac{\phi}{2+\phi}(V^n - V^{n-1}) + \frac{2\Delta t}{2+\phi}\{\theta\psi^{n+1} + (1-\theta)\psi^n\} \tag{13}$$

where the net volume swept by the cell, ψ, is defined by

$$\psi = (\xi_t\Delta S)_{i+1/2} - (\xi_t\Delta S)_{i-1/2} + (\xi_t\Delta S)_{j+1/2} - (\xi_t\Delta S)_{j-1/2} + (\xi_t\Delta S)_{k+1/2} - (\xi_t\Delta S)_{k-1/2} \tag{14}$$

The computational method used in this paper has been extensively validated for a number of unsteady flows in which the deforming-mesh method was applied to the oscillatory motion of wings and airfoils. The details of this validation can be found in [25].

V. Computations of Flows Induced by Synthetic Jets

A. Case 1 of the CFDVAL2004 Workshop

Case 1 of the CFDVAL2004 workshop is chosen as the first example to show the accuracy of the current method. A diaphragm located on the left side of the cavity of a synthetic jet oscillating at a frequency of 450 Hz creates an alternating incoming and outgoing flow through the cavity and the neck, resulting in a jet of net zero mass flow rate. The jet comes out of the slot and interacts with the surrounding quiescent air. Even though the aspect ratio of the slot is 28, the end effects of the slot were found to be prominent [26]. In this paper, therefore, we conduct a three-dimensional simulation with a three-dimensional multiblock-structured grid system. The grid system with which the end effects of the slot can be calculated was downloaded from the website of the CFDVAL2004 workshop. However, the block structure of the grid system is reorganized so that the automatic generation of the grid can be done more easily. Only the blocks inside the cavity are allowed to deform as the diaphragm moves, while the other blocks are kept unchanged. The total number of grid points is approximately 4.3 million. Cui and Agarwal [10] conducted a grid-convergence study by doubling the grid resolution of a baseline-grid system of the external flow region in the y direction. The number of grid points of the baseline-grid system was slightly more than half a million, which is quite coarse when compared with the grid system used in this paper. They, however, concluded that their solution using the baseline-grid system was grid independent.

A characteristic far-field boundary condition is applied along the left, right, and top sides of the exterior flow domain, while a nonslip boundary condition is imposed at the diaphragm, the walls of the actuator including the nozzle neck, and the bottom of the exterior

field. The movement of the circular diaphragm is modeled with the solution, $u(r, t)$, to a two-dimensional wave equation:

$$\frac{\partial^2 u}{\partial t^2} = c^2\left(\frac{\partial^2 u}{\partial r^2} + \frac{1}{r}\frac{\partial u}{\partial r}\right) \tag{15}$$

with the initial conditions

$$u(r, 0) = A(R^2 - r^2), \qquad u_t(r, 0) = 0 \tag{16}$$

and the boundary condition

$$u(R, t) = 0 \quad \text{for all } t \geq 0 \tag{17}$$

The initial and the boundary conditions imply that the membrane is fixed along the boundary of the diaphragm, $r = R$, and that the initial condition is the maximum displacement of the membrane. The value of A is determined so that the experimental peak velocity is matched. If the stroke of the diaphragm had been known, no numerical test would have been required to determine the value of A. Using the method of separation of variables, the solution that satisfies the initial and the boundary conditions is found to be

$$u(r, t) = \sum_{m=0}^{\infty} a_m J_0\left(\alpha_m \frac{r}{R}\right) \cos \alpha_m c t \tag{18}$$

where J_n is the nth order of the Bessel function, and α_m is the zero of the Bessel function. The coefficients of the Fourier–Bessel series, a_m, are given as the following equation:

$$a_m = \frac{2}{R^2 J_1^2(\alpha_m)} \int_0^R r f(r) J_0\left(a_m \frac{r}{R}\right) \mathrm{d}r \tag{19}$$

The Reynolds number, based on the peak jet velocity and the width of the slot, is 2800. The number of the subiterations for the dual time-stepping method is set to 60. To remove any transient behavior of the solution, 10 periods of computation are performed, and the last two periods are used for comparison with the experimental data. Time-accurate computations are done at every 0.5 deg phase angle, which results in 720 time-accurate computations over one period. A simple trapezoidal integration of the solution over the two periods is used to obtain the time-averaged solution.

In Fig. 1a, the vertical velocity profile at the slot center is plotted over a cycle. This figure is used to determine the amplitude of the oscillation of the diaphragm. Figure 1b depicts the time average of the vertical velocity profile over a period. In these figures, the experimental results measured with particle image velocimetry (PIV) and laser Doppler velocimetry (LDV) are presented for comparison. Furthermore, the two-dimensional results of Park et al. [9], Cui and Agarwal [10], and Yoo et al. [13] are presented. Park et al. [9] used a transpiration boundary condition in which a periodic blowing-and-suction velocity was specified at the end of the neck, and Cui and Agarwal [10] used a simple periodic boundary condition in which a simple sinusoidal velocity was specified at the diaphragm. On the other hand, Yoo et al. [13] adopted the two-dimensional exact model for their computation so that the jet velocity profile and its magnitude were parts of the solution. From the figures, it can be seen that the results with the three-dimensional exact jet model match the shape of the vertical velocity history more closely than do the results of any other methods. Although the simple periodic boundary condition specified at the diaphragm matches the time-averaged vertical velocity profile best, it does not follow the time history at the center of the jet of the experiment. The magnitude of the averaged vertical velocity increases due to counter-rotating vortices generated at the expulsion stage. These vortices dissipate as they move upward. All the computational results capture the essential physics of the synthetic jet. Figure 2 presents the phase-averaged vertical velocity components along the vertical distance at $y = 1$ and 4 mm. The three-dimensional exact model produces the best results for the jet width, whereas the transpiration boundary-condition model produces the worst results. Both the two-dimensional and the three-dimensional exact models give considerably similar results.

The z-vorticity contour plots at every 90 deg at the midspan are presented in Fig. 3. From these figures, the formation and the evolution of vortices due to the synthetic jets can be seen. When the jet is blowing out of the neck, shear layers are formed between the ejected air and the quiescent air due to the velocity difference. At the end of the blowing phase, these layers roll up and form a pair of vortices. During the suction phase, the air is sucked into the actuator cavity, but the vortices generated during the blowing phase have convected out far enough away from the neck that they do not come back into the cavity. It is noticeable that the vortices are formed through the nozzle neck as the shear layers develop due to the interaction between the air sucked in and the air remaining. In addition, a shear layer on the diaphragm is found throughout the complete strokes. Unsteady complex interactions between the vortices and the shear layers exist inside the cavity. Therefore, it is necessary to include the cavity and the stroke of the diaphragm in the computation for an accurate simulation of the synthetic jet flow rather than to omit them for the sake of computational efficiency.

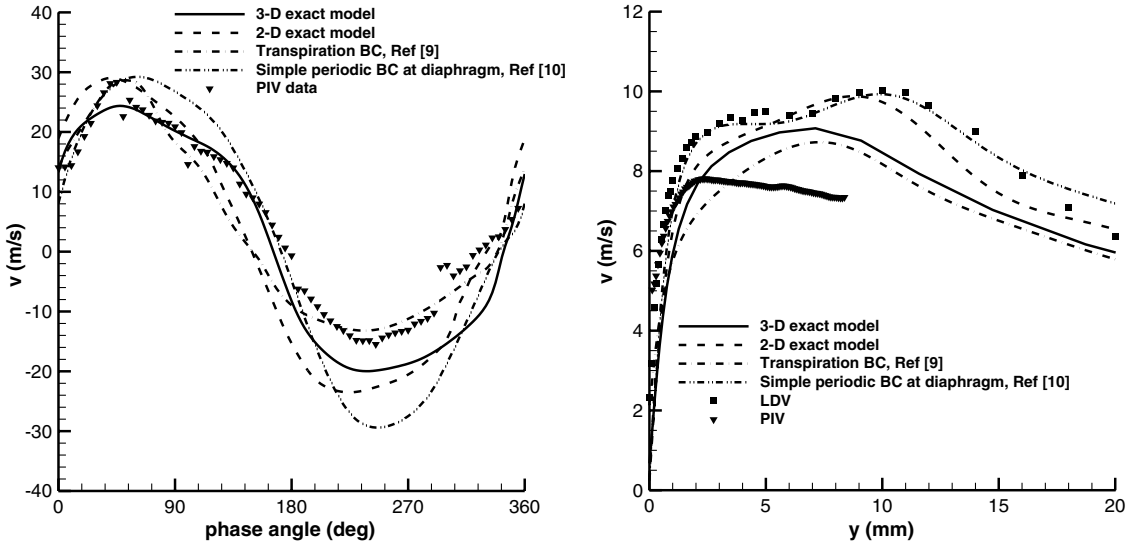

a) Phase averaged vertical velocity component

b) Time averaged vertical velocity component

Fig. 1 Vertical velocity profiles near the slot exit component (3-D denotes three-dimensional, 2-D denotes two-dimensional, and BC denotes boundary control).

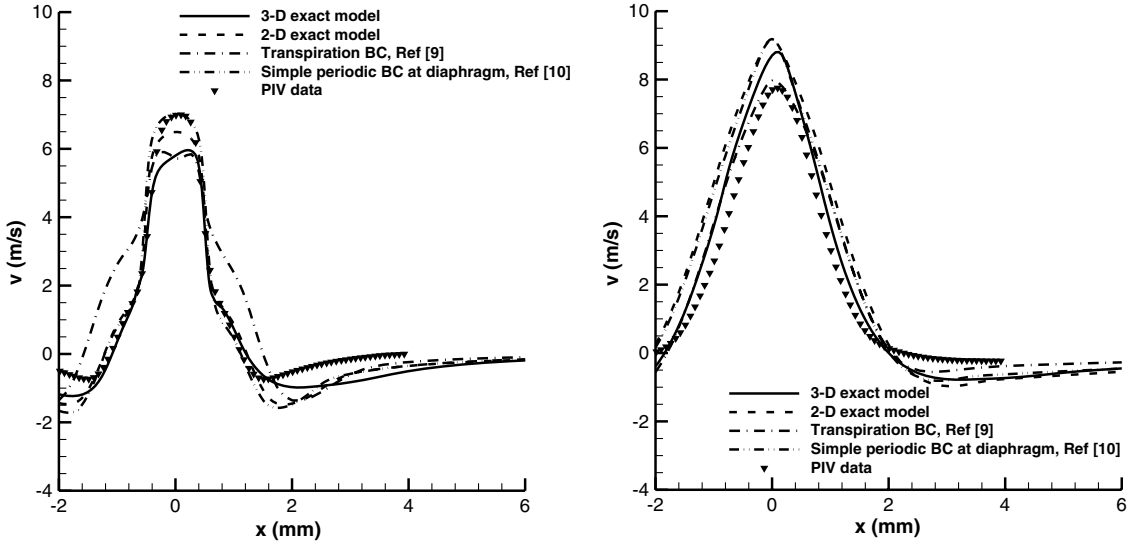

Fig. 2 Time-averaged vertical velocity components.

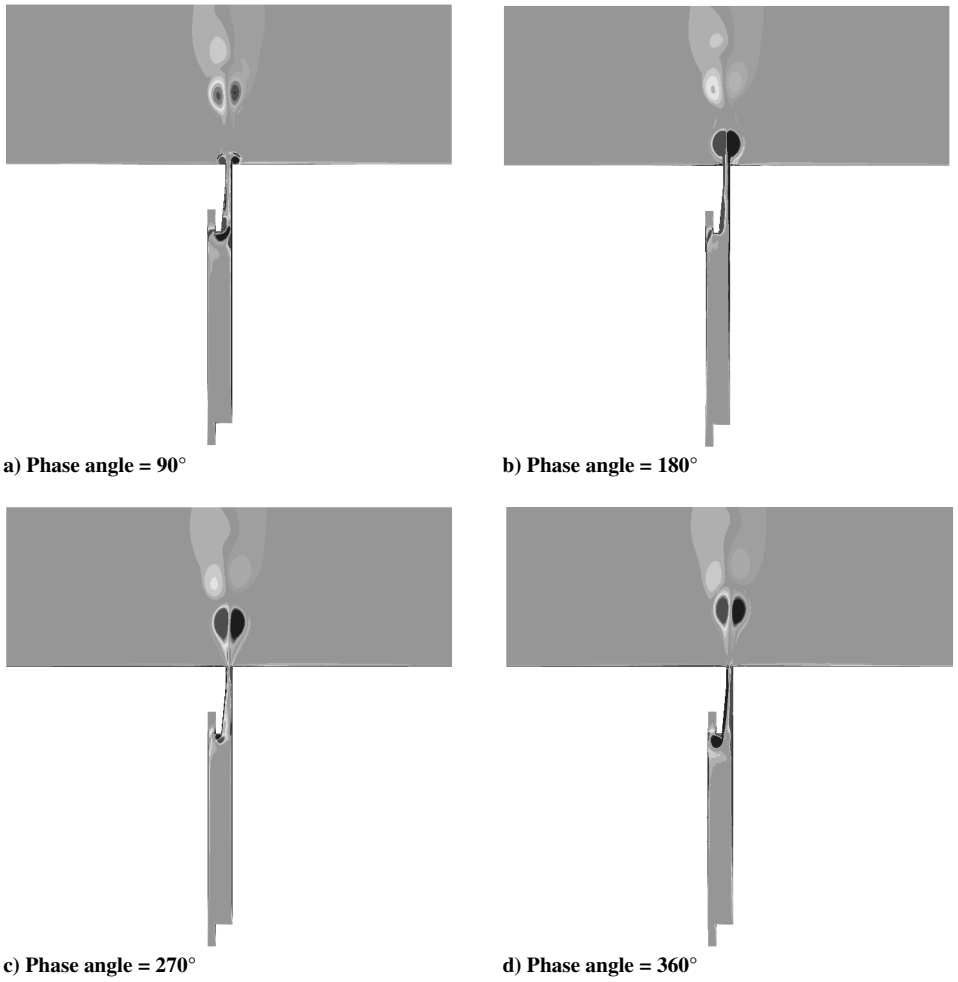

Fig. 3 Phase-averaged vorticity contour plots.

Figure 4 presents the time-averaged vertical velocity component contour plots in planes normal and parallel to the slot. Figure 4a shows that the jet maintains its integrity until $y = 12$ mm, and suddenly gets wider due to viscous diffusion as found in Yao et al.'s experiment [26]. The three-dimensionality of the flow can be seen much more clearly in Fig. 4b. The edge effect begins to move toward the center of the jet. These contour plots confirm Yao et al.'s finding that the end effects become significant above approximately $8h$, where h is the width of the slot. Figure 5 shows four streamline plots of the phase-averaged synthetic flowfields in the plane parallel to the slot. In this figure, the ends of the slot are located at ± 16.8 mm. At 90 deg, a pair of vortices forms near the end of the slot. Subsequently, they move upward with the jet as the phase angle increases to 180 deg. At the same time, the suction phase begins. The centers of

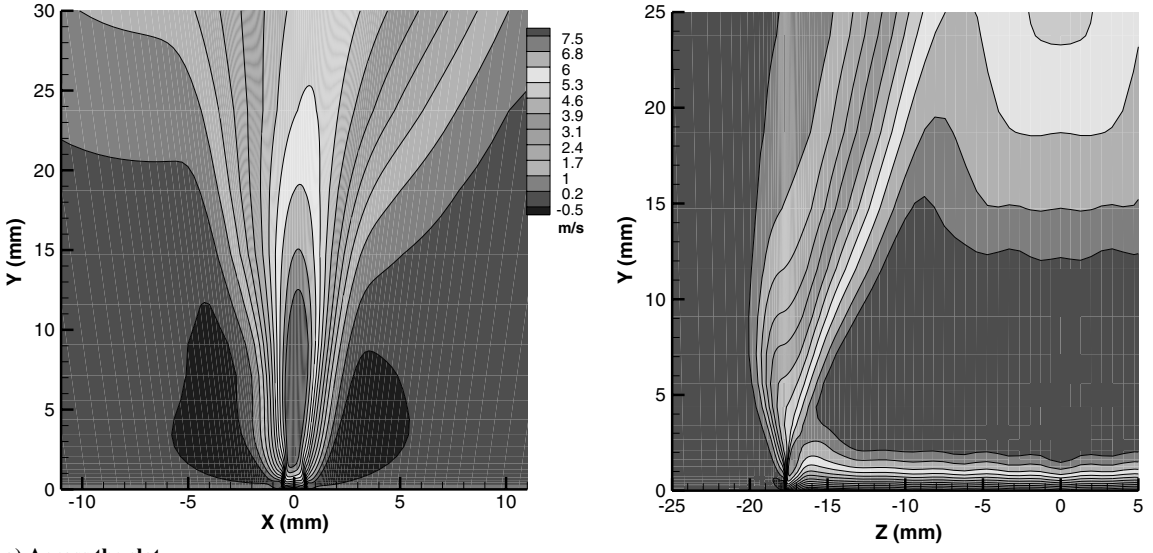

a) Across the slot

b) Along the slot

Fig. 4 Time-averaged vertical velocity component contour plots.

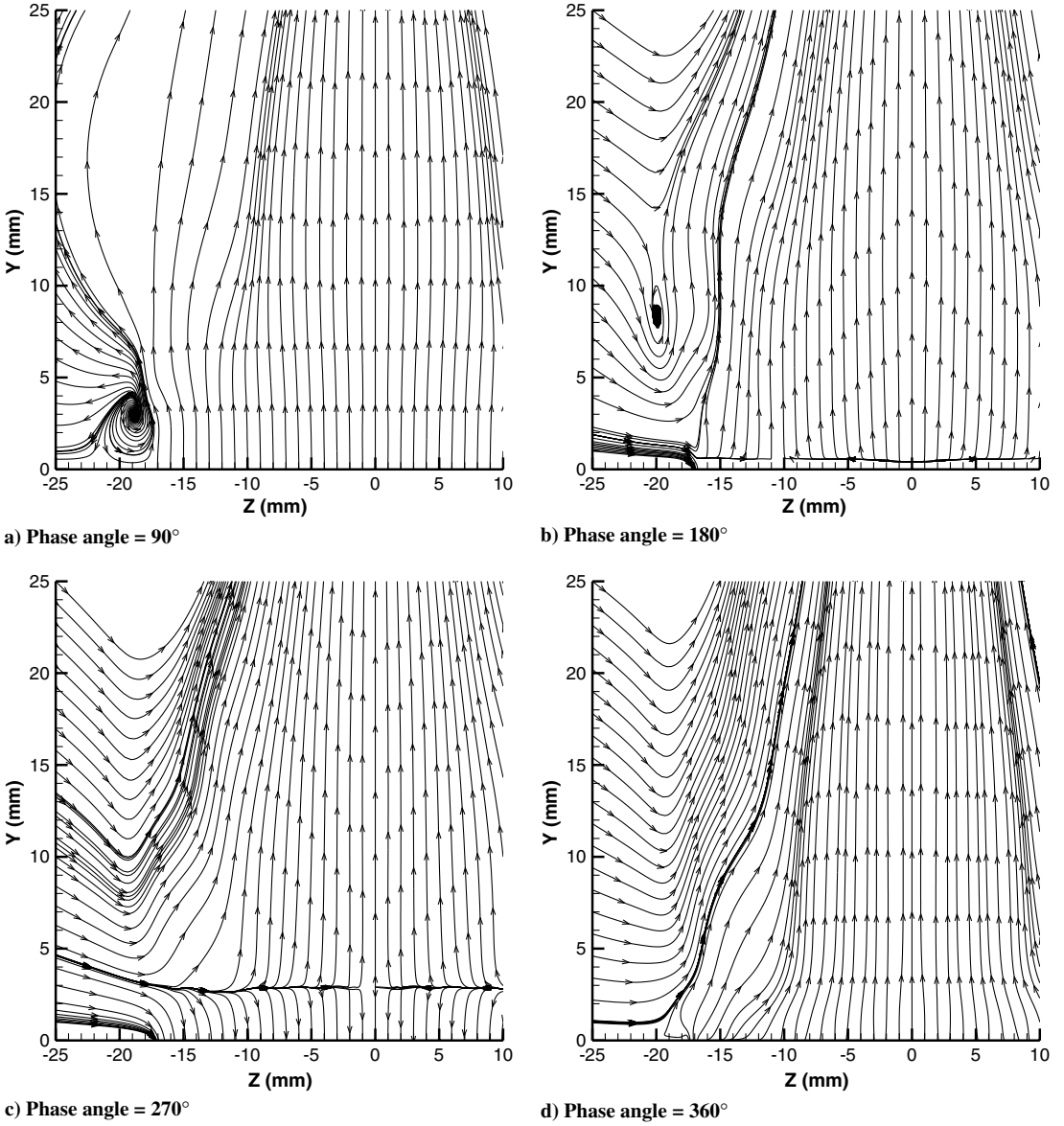

a) Phase angle = 90°

b) Phase angle = 180°

c) Phase angle = 270°

d) Phase angle = 360°

Fig. 5 Phase-averaged streamline plots along the slot.

the vortices, however, are located slightly farther outside than those found in Yao et al.'s experiment. The suction region extends upward at 270 deg. As can be seen from the 360 deg phase streamline plot, the edge effect penetrates deeper into the center of the jet.

B. Case 2 of the CFDVAL2004 Workshop

The next computational example with the three-dimensional exact model is case 2 of the CFDVAL2004 workshop. Unlike the previous example, this is a truly three-dimensional flow. Schaeffler and Jenkins conducted an experimental study of the flow [27,28]. A synthetic jet through a circular orifice meets with a turbulent crossflow. The synthetic jet is produced by the mechanical operation of a rectangular piston that is located at the bottom of a cavity. A flexible membrane is attached to the piston. The membrane moves up and down as the piston is oscillated with a frequency of 150 Hz. The oscillating motion of the synthetic jet device consists of the rigid motion of the piston and the elastic motion of the membrane. The freestream is a fully developed turbulent flow with a boundary-layer thickness of 21 mm. The freestream Mach number is 0.1. The Reynolds number, based on the flow velocity and the diameter of the orifice, is 14,150.

A block-structured grid is obtained from the workshop webpage. The grid system has 28 blocks; the total number of grid points is approximately 4.09 million. The wall spacing is no greater than 10^{-4} mm, which is the value of the original grids. The spacing is reasonably small for the RANS simulation. Rumsey [29] conducted a grid convergence test using the same grid system. He concluded that the effect of grid refinement was small when compared to the difference between the computational results and experimental data. Because no other boundary-layer parameters except the boundary-layer thickness are given at the inflow boundary, the problem of a turbulent flow over a flat plate is solved numerically. The velocity components, the temperature, and the turbulent flow variables at the inflow boundary are specified with those determined from the computation. The pressure, however, is extrapolated from the computational domain. A nonreflecting far-field boundary condition is specified at the outer boundaries except for the bottom wall. A nonslip condition is specified along the bottom surface of the outer region as well as along the boundary surfaces of the jet actuator. The number of inner time steps for the dual time step is set to 60. The number of time-accurate computations made per cycle is 720, as in the previous case. For the unsteady computation, more than four cycles are required for the periodic solutions.

The streamwise and the vertical velocity distributions at the orifice exit are plotted in Fig. 6. The vertical velocity component in Fig. 6b is used to determine the amplitude of the oscillating piston so that the peak of the vertical velocity is $1.5U_\infty$ [11]. The experimental data and the computational results of Rumsey [29] are presented for comparison. Rumsey used the K-ω SST turbulence model for the turbulent viscosity computation, and a three-dimensional version of Cui's boundary model [11] as a synthetic jet boundary condition. Our computational results are in good agreement with the experimental data as well as with Rumsey's results. Figure 7 shows the time-averaged velocity components at $1D$ upstream and $2D$ downstream of the nozzle exit in the center plane. Here, D is the diameter of the nozzle exit. The figures show that the three-dimensional exact model performs well in predicting the velocity profile at the center plane. Figure 8 depicts the phase-averaged velocity components at the phase angle of 80 deg. Figure 8 indicates that the computational results with the three-dimensional exact model are in close agreement with the experimental results at $1D$ downstream and $8D$ downstream of the nozzle exit. Comparisons of the contour plots from the CFD results and the PIV results are made in Fig. 9. This figure presents the time-averaged streamwise velocity contour plots on the y-z plane at $4D$ downstream. The in-plane velocity vector is also plotted using the velocity components in the y and z directions. In the figure, a pair of counter rotating vortices formed around $z = 9$ mm is well captured in the computation. Furthermore, the distance between the vortex centers is predicted and found to be very close to that of the measured PIV data. It is noticeable that the vortices of the PIV data look asymmetric whereas the CFD result shows that the pair of vortices is fairly symmetric. In Fig. 10, the phase-averaged streamwise velocity contour plots are presented at $1D$ downstream and in the center plane when the piston moves upward. As can be seen in the figures, the freestream is perturbed by the outgoing jet near the exit of the orifice. Although the contours show a flow structure that is very similar to that of the experimental data, the experimental result seems to be asymmetric and is inclined to the left. On the other hand, the computation shows a very small sign of asymmetry, as found in [29]. The asymmetry found in the experiment could be related to the instability found in a steady jet in crossflow. A strong enough steady jet flowing into a crossflow oscillates due to flow instability [30]. Similar instability could occur in a synthetic jet in crossflow. Figure 11 exhibits the phase-averaged streamwise velocity component in the center plane. The figure clearly shows that the jet bends due to the freestream.

C. Case 3 of the CFDVAL2004 Workshop

The last computational example that uses deforming mesh is case 3 of the CFDVAL2004 workshop. The original experiment of Seifert

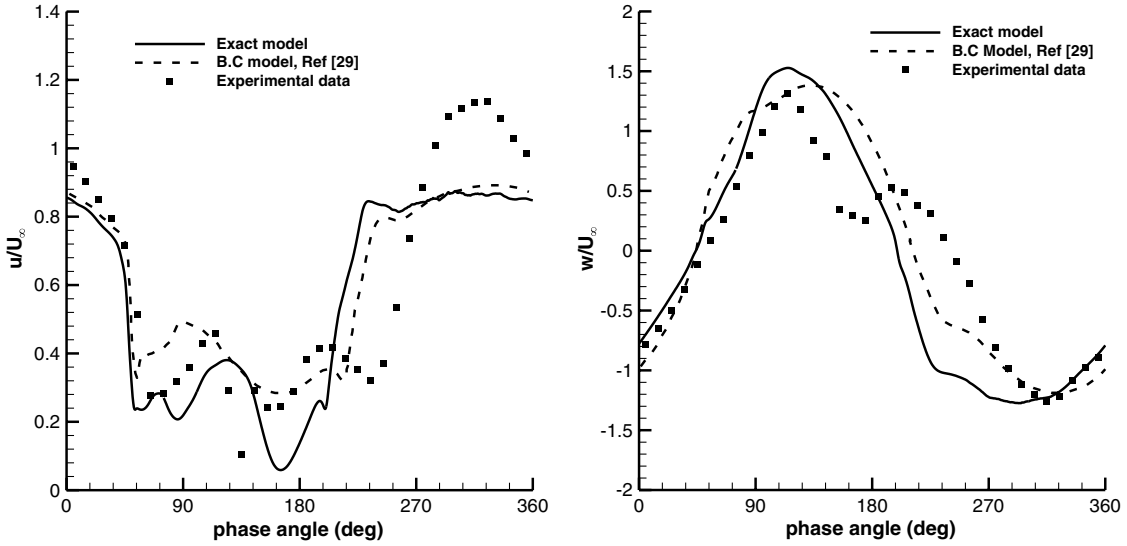

a) Streamwise velocity profiles b) Vertical velocity profiles

Fig. 6 Phase-averaged velocity profiles at the nozzle exit.

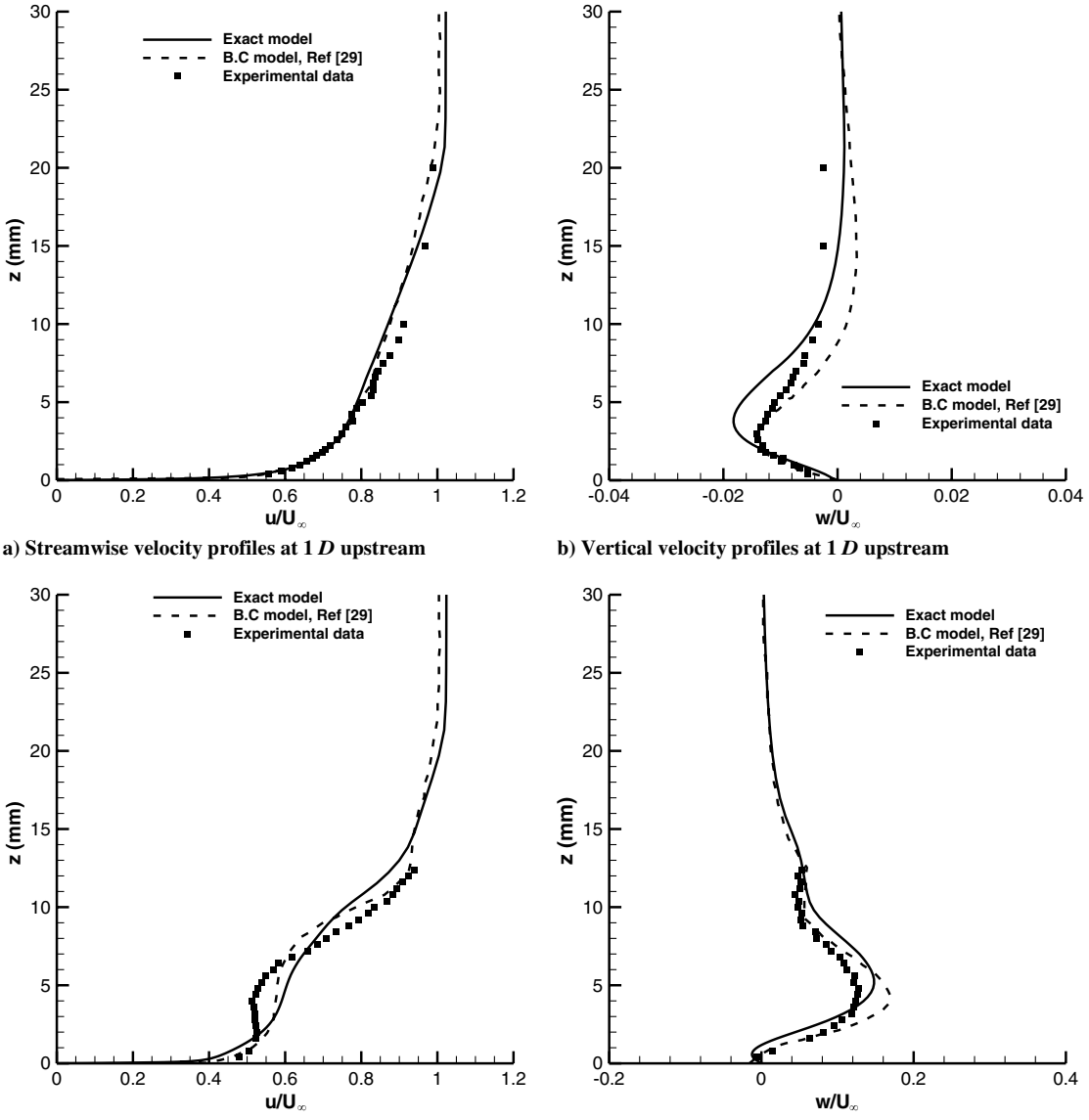

a) Streamwise velocity profiles at 1 D upstream

b) Vertical velocity profiles at 1 D upstream

c) Streamwise velocity profiles at 2 D downstream

d) Vertical velocity profiles at 2 D downstream

Fig. 7 Time-averaged velocity profiles at 1D upstream and 2D downstream of the nozzle exit.

and Pack [31] was repeated by Greenblatt et al. [32,33] to provide a complete data set that can be easily used for CFD validation. They investigated the flow over a wall hump with oscillatory control and steady suction or blowing. Oscillatory control was achieved with a zero-efflux oscillatory jet introduced from the spanwise slot. The model was mounted between two glass endplates, and both leading and trailing edges were faired smoothly with a wind tunnel splitter plate. It should be noted that the flow is two-dimensional except near the endplates where sidewall effects exist [34]. Thus, a two-dimensional RANS calculation is performed and a computational geometry with a top wall shape is chosen to account for the blockage effect, as was done by Rumsey [34]. The Reynolds number is one million based on the chord length of the hump, c, and the freestream velocity. The movement of the diaphragm is modeled in a manner similar to that used in case 2, in which the motion consists of rigid and flexible motions. The diaphragm is oscillated with a frequency of 138.5 Hz, and the maximum velocity at the orifice exit is approximately 27 m/s. Rumsey [34] also investigated the effect of grids on the flow. He concluded that grid 5 given on the workshop homepage was sufficient to adequately resolve the flow feature of the hump model flow using URANS. The grid contains five zones and 53,013 grid points. For a time-accurate simulation, 720 computations are made over a cycle and 60 inner time steps are used for the dual time stepping. To obtain a periodic solution, more than ten cycles of calculations are performed. Only the last cycle is used to calculate the mean-time solutions for the comparison with the experimental data. A nonslip boundary condition is specified at the floor and hump surfaces, as well as at the solid walls inside the cavity. A fully developed turbulent flow with a boundary-layer thickness of $\delta/c = 0.073$ is specified at $x/c = -6.39$. A far-field boundary condition is applied at the downstream boundary. The upper wall is treated as inviscid. According to Rumsey's research, the use of either an inviscid or a viscous boundary condition on the top wall made little difference [34]. A nonslip wall boundary condition is also specified at the bottom of the cavity in the exact model.

In Fig. 12, the time-averaged surface pressure coefficients are plotted along with the experimental result as well as with the result for the boundary-condition model [34]. The figure shows the development of an adverse pressure gradient before the leading edge of the hump, the acceleration of the flow to $x/c = 0.5$ and another relatively strong adverse pressure gradient that develops before the location of flow separation at $x/c = 0.65$. The large spike in the pressure coefficient distribution at the slot is caused by flow acceleration around the upstream edge of the slot lip. The computational results for the exact model as well as for the boundary-condition model agree well with the experimental data. The results

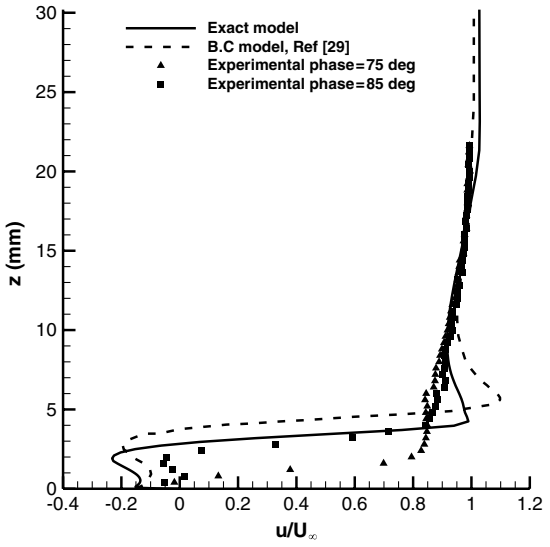

a) Streamwise velocity profiles at 1 *D* downstream

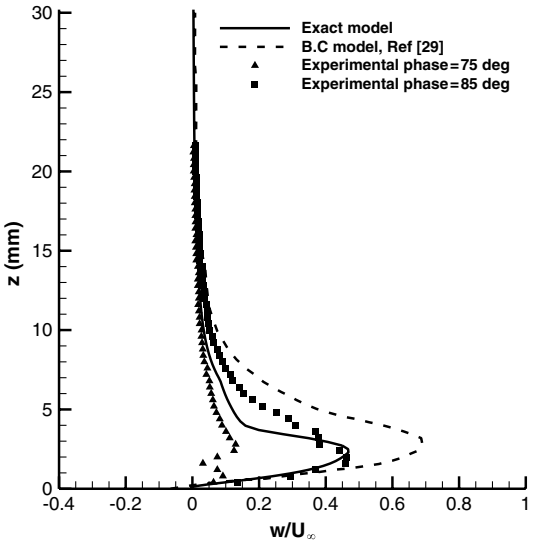

b) Vertical velocity profiles at 1 *D* downstream

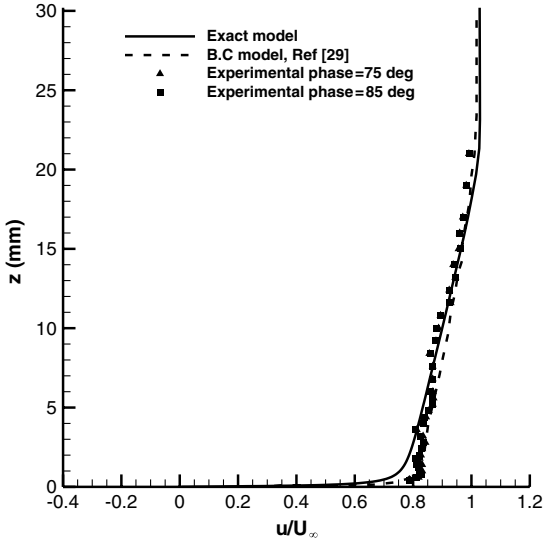

c) Streamwise velocity profiles at 8 *D* downstream

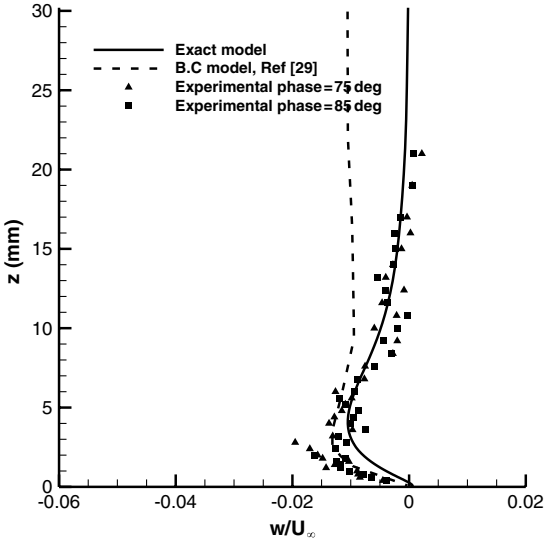

d) Vertical velocity profiles at 8 *D* downstream

Fig. 8 Phase-averaged velocity profiles at 1*D* downstream and 8*D* downstream of the nozzle exit, phase angle = 80 deg.

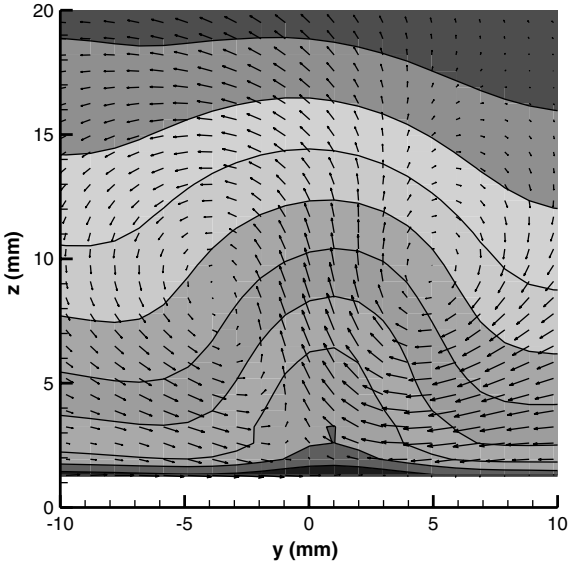

a) PIV measurement

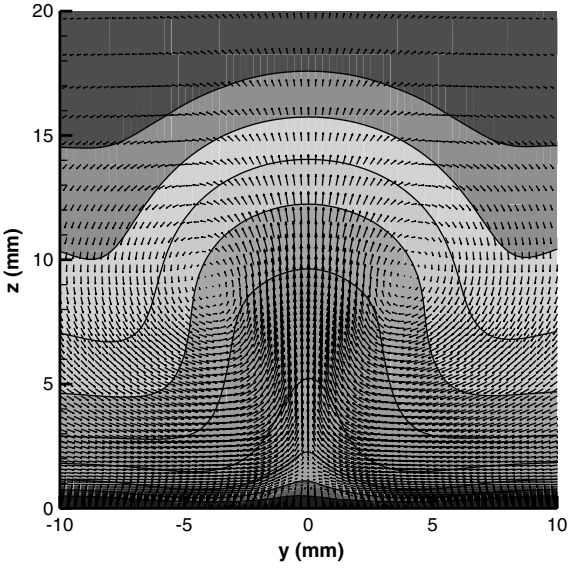

b) Computational result

Fig. 9 Time-averaged streamwise velocity contour plots And in-plane velocity vector plots at 4*D* downstream of the nozzle exit.

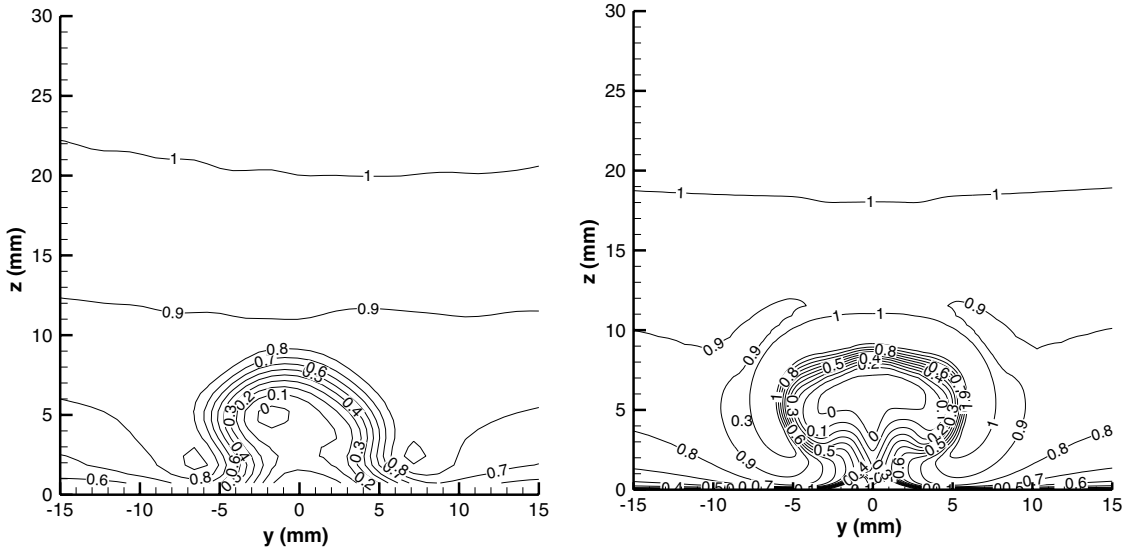

a) PIV measurement b) Computational result

Fig. 10 Phase-averaged streamwise velocity contour plots at 1*D* downstream of the nozzle exit, phase angle = 120 deg.

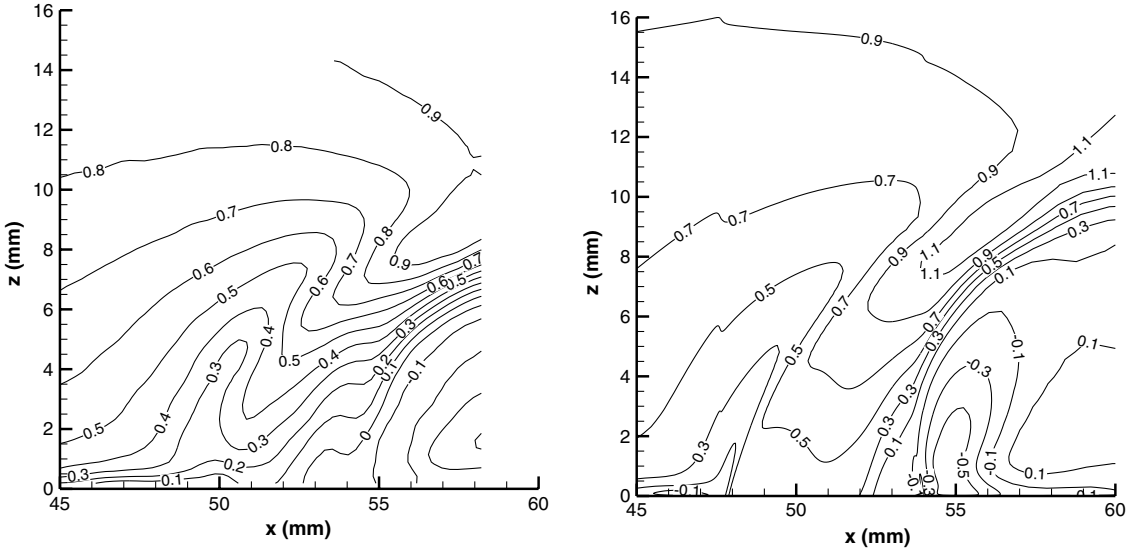

a) PIV measurement b) Computational result

Fig. 11 Phase-averaged streamwise velocity contour plots at the center plane, phase angle = 120 deg.

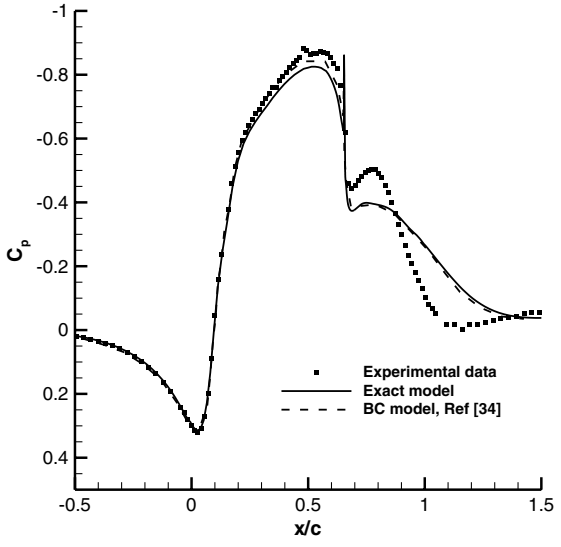

Fig. 12 Time-averaged surface pressure coefficient distributions.

for the exact model are almost identical to the results for the simple boundary-condition model. Some differences, however, exist in the pressure coefficient distributions between the computations and the experimental data for the separation region. The time-averaged streamlines are illustrated in Fig. 13. Although the separation point is relatively well predicted by the method, the reattachment point is not. Table 1 summarizes the separation points and the reattachment points predicted by the numerical methods.

The computational results with the exact model for three cases of the CFDVAL2004 workshop suggest that the effect of the boundary-condition model is not the sole source of uncertainty in the synthetic jet flow computations. Rumsey conducted a computational experiment in his URANS computation of case 3 in which the turbulence viscosity was intentionally doubled inside the separation bubble. The modification drastically improved the prediction of the reattachment point. Therefore, he concluded that the deficiency in the standard turbulence model was likely to blame for the overpredicted bubble size. The results of his numerical experiment can also be interpreted in such a way as to say that the effect of the turbulence model would be another source of uncertainty in the synthetic jet flow computations. It would be an interesting research topic to compute

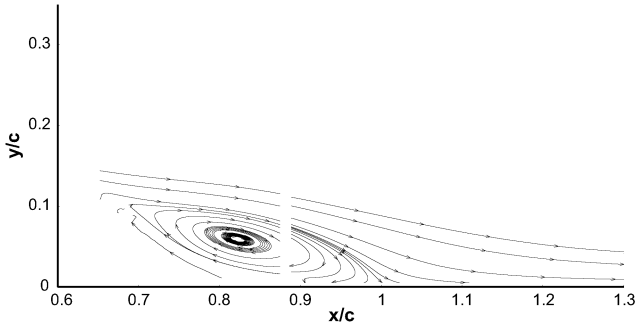

a) Experimental result

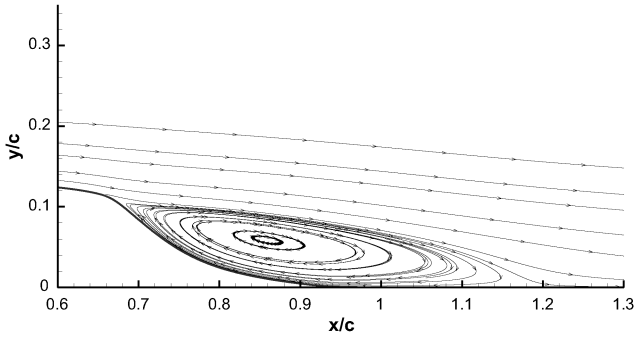

b) Computational result

Fig. 13 Time-averaged streamlines.

Table 1 Separation and reattachment points

Condition	Model	Separation point (x/c)	Reattachment point (x/c)
Experiment		0.67	0.99
Oscillatory (mean)	[34]	0.663 (1.0%)	1.22 (23.2%)
Oscillatory (mean)	Exact model	0.664 (0.9%)	1.20 (21.2%)

synthetic jet flows with high-order turbulence models such as large eddy simulation (LES) or hybrid RANS-LES models in conjunction with the exact model with deforming mesh.

The vorticity contour plots are presented in Fig. 14 at two phase angles. It is clear that the vortices generated by the jet are convected downstream and dissipated. The repeated process of vortex roll-up and shedding is known to effectively reduce the separation bubble size [34]. Figure 15 shows the phase-averaged pressure coefficients behind the hump at the same phases as those in the previous figure. The computational results predict the strength and location of the shed vortices well. However, the pressure coefficient levels tend to be somewhat lower in magnitude than the measured values for $0.65 < x/c < 0.8$ and higher than the measured values for $0.95 < x/c < 1.1$.

Figure 16 shows the phase-averaged streamwise velocity profiles at three locations. At $x/c = 0.66$, which is just downstream of the slot, the flow is still attached in the time mean. At the blowing phase of 170 deg, the velocity profile indicates that the flow near the slot is perturbed by the influence of the fluid expulsion from the slot. The velocity at an inflection of the profiles is underpredicted at both phases. At $x/c = 0.8$, which is in the middle of the separation region, the computations predict the velocity profiles well. At $x/c = 1.0$, the computational velocity profiles indicate that the flow still remains separated, but the experimental result indicates that the flow has just attached. This disagreement can be understood to stem from the difference in the location of the flow reattachment, as can be seen in Fig. 13.

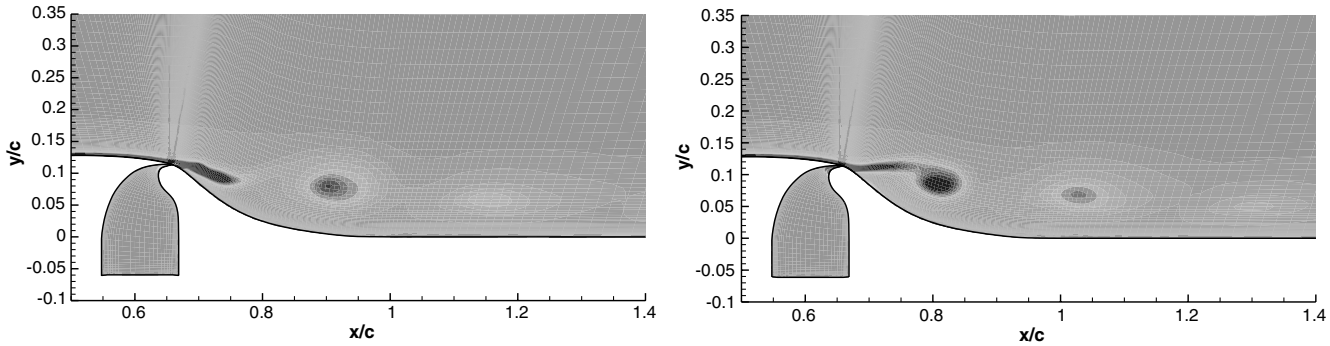

a) Phase angle = 170° **b) Phase angle = 350°**

Fig. 14 Instantaneous vorticity contour plots.

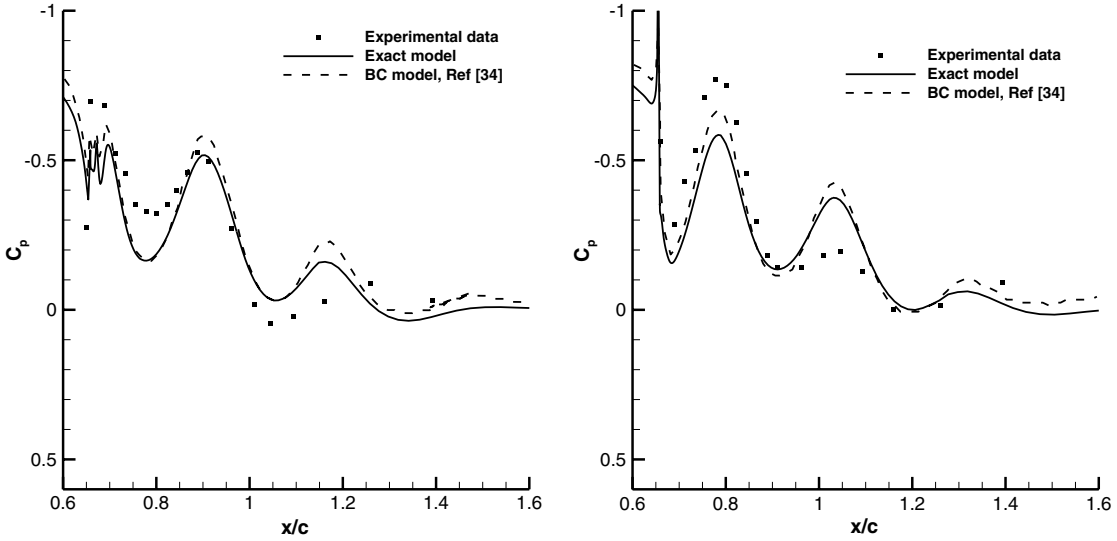

a) Phase angle = 170° b) Phase angle =350°

Fig. 15 Phase-averaged pressure coefficient distributions.

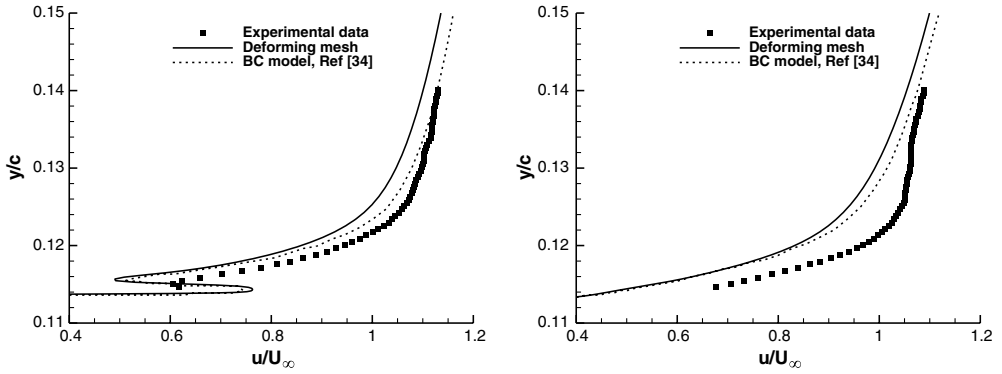

a) Phase angle = 170°, x/c=0.66 b) Phase angle = 350°, x/c=0.66

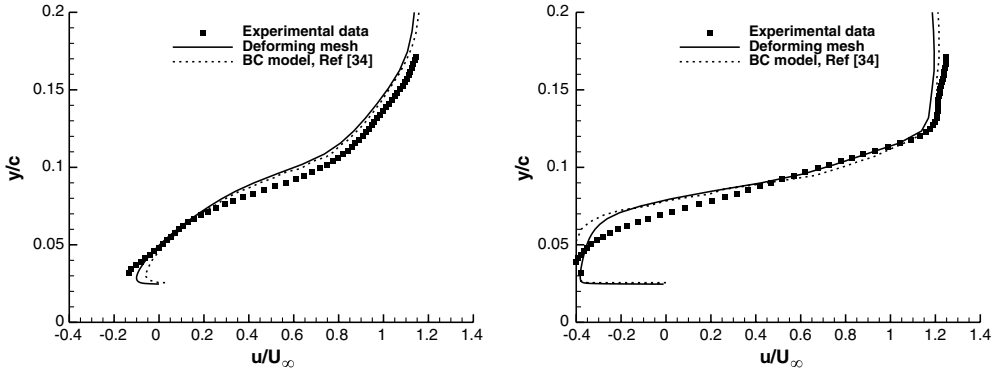

c) Phase angle = 170°, x/c=0.8 d) Phase angle = 350°, x/c=0.8

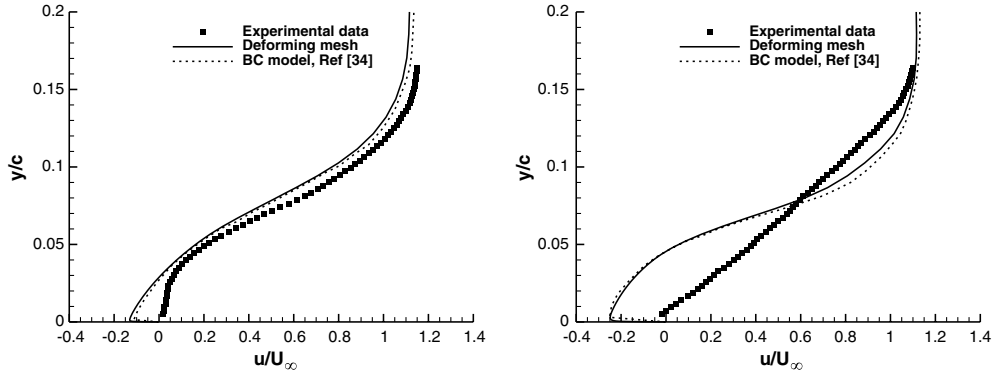

e) Phase angle = 170°, x/c=1.0 f) Phase angle = 350°, x/c=1.0

Fig. 16 Phase-averaged streamwise velocity profiles.

VI. Conclusions

In this paper, simulations using deforming mesh for synthetic jet flows into quiescent air, into a turbulent crossflow, and into a turbulent separated flow over a hump were discussed. To facilitate the deformation of mesh inside the cavity of a real jet actuator, a transfinite interpolation method was used. With the automatic grid generation, the time-dependent Reynolds-averaged Navier–Stokes equations were solved for the flowfield induced by synthetic jets. Simultaneously, the volumes of the deforming cells were evaluated using the geometric conservation law. All three cases of the Langley Research Center Workshop Computational Fluid Dynamics Validation of Synthetic Jets and Turbulent Separation Control workshop were successfully computed using the deforming mesh without any boundary-condition models. The computed results were shown to be in good agreement with the previously published results, as well as with the experimental results. The three-dimensionality due to the edge effect of the slot in case 1 was computationally confirmed. Also, it was suggested that a high-order turbulence model such as large eddy simulation or hybrid Reynolds-averaged Navier–Stokes–large eddy simulation should be employed in conjunction with the exact model.

Acknowledgment

This work was supported by Inha University, the Defense Acquisition Program Administration, and the Agency for Defense Development.

References

[1] Smith, B. L., and Glezer, A., "The Formation and Evolution of Synthetic Jets," *Physics of Fluids*, Vol. 10, No. 9, 1998, pp. 2281–2297.

[2] Smith, B. L., and Glezer, A., "Jet Vectoring Using Synthetic Jets," *Journal of Fluid Mechanics*, Vol. 458, 2002, pp. 1–34.

[3] Chen, Y., Liang, S., Aung, K., Glezer, A., and Jagoda, J., "Enhanced Mixing in a Simulated Combustor Using Synthetic Jet Actuators," AIAA Paper 1999-0449, Jan. 1999.

[4] Smith, D. R., Amitay, M., Kibens, V., Parekh, D. E., and Glezer, A., "Modification of Lifting Body Aerodynamics Using Synthetic Jet Actuators," AIAA Paper 1998-0209, Jan. 1998.

[5] Rumsey, C. L., Gatski, T. B., Sellers, W. L., Vatsa, V. N., and Viken, S. A., "Summary of the 2004 CFD Validation Workshop on Synthetic Jets and Turbulent Separation Control," AIAA Paper 2004-2217, June 2004.

[6] Rumsey, C. L., "Successes and Challenges for Flow Control Simulations (Invited)," AIAA Paper 2008-4311, June 2008.

[7] Yamaleev, N. K., and Carpenter, M. H., "A Quasi-1-D Model for Arbitrary 3-D Synthetic Jet Actuators," *AIAA Journal*, Vol. 44, No. 2, 2006, pp. 208–216. doi:10.2514/1.14495

[8] Vatsa, V. N., and Turkel, E., "Simulation of Synthetic Jets in Quiescent Air Using Unsteady Reynolds Averaged Navier–Stokes Equations," *AIAA Journal*, Vol. 44, No. 2, 2006, pp. 217–224. doi:10.2514/1.13535

[9] Park, S. H., Yu, Y. H., and Byun, D. Y., "RANS Simulation of a Synthetic Jet in Quiescent Air," AIAA Paper 2007-1131, Jan. 2007.

[10] Cui, J., and Agarwal, R. K., "3D CFD Validation of a Synthetic Jet in Quiescent Air (NASA Langley Workshop Validation: Case 1)," AIAA Paper 2004-2222, June 2004.

[11] Cui, J., and Agarwal, R. K., "3D CFD Validation of an Axisymmetric Jet in Cross-flow (NASA Langley Workshop Validation: Case 2)," AIAA Paper 2005-1112, Jan. 2005.

[12] Balakumar, P., "Computations of Flow over a Hump Model Using High Order Method with Turbulence Modeling," AIAA Paper 2005-1270, Jan. 2005.

[13] Yoo, I., Lee, S., Kim, W., and Kim, C., "Boundary Condition Models for Synthetic Jet Simulation," AIAA Paper 2010-1413, Jan. 2010.

[14] Weiss, J. M., and Smith, W. M., "Preconditioning Applied to Variable and Constant Density Flows," *AIAA Journal*, Vol. 33, No. 11, 1995, pp. 2050–2057. doi:10.2514/3.12946

[15] Menter, R., "Two-Equation Eddy-Viscosity Turbulence Models for Engineering Applications," *AIAA Journal*, Vol. 32, No. 8, 1994, pp. 1598–1605. doi:10.2514/3.12149

[16] Roe, R. L., "Approximate Riemann Solvers, Parameter Vectors and Difference Schemes," *Journal of Computational Physics*, Vol. 43, No. 2, 1981, pp. 357–372. doi:10.1016/0021-9991(81)90128-5

[17] Van Leer, B., "Towards the Ultimate Conservative Difference Scheme. V. A Second Order Sequel to Godunov's Method," *Journal of Computational Physics*, Vol. 32, No. 1, 1979, pp. 101–136. doi:10.1016/0021-9991(79)90145-1

[18] Beam, R. M., and Warming, R. F., "Factored, A-Stable, Linear Multistep Methods: an Alternative to the Method of Lines for Multidimensions," *ACM-SIGNUM Newsletter*, Vol. 14, No. 3, Sept. 1979, pp. 17–19.

[19] Merkle, C. L., and Athavale, M., "Time-Accurate Unsteady Incompressible Flow Algorithms Based on Artificial Compressibility," AIAA Paper 1987-1137, June 1987.

[20] Beam, R. M., and Warming, R. F., "Implicit Numerical Methods for the Compressible Navier–Stokes and Euler Equations," von Kármán Institute for Fluid Dynamics Lecture Series, von Kármán Institute for Fluid Dynamics, Rhode Saint Geneses, Belgium, 1982.

[21] Lee, S., and Choi, D. W., "On Coupling the Reynolds-Averaged Navier–Stokes Equations with Two-Equation Turbulence Model Equations," *International Journal for Numerical Methods in Fluids*, Vol. 50, No. 2, Jan 2006, pp. 165–197. doi:10.1002/fld.1049

[22] Thompson, J. F., Soni, B. K., and Weatherill, N. P., *Handbook of Grid Generation*, 1st ed., CRC Press, Boca Raton, FL, 1998, Part 1-3-1.

[23] Soni, B. K., "Two- and Three-Dimensional Grid Generation for Internal Flow Applications of Computational Fluid Dynamics," AIAA Paper 1985-1526, July 1985.

[24] Thomas, P. D., and Lombard, C. K., "The Geometric Conservation Law: A Link Between Finite-Difference and Finite-Volume Methods of Flow Computation on Moving Grids," AIAA Paper 1978-1208, July 1978.

[25] Yoo, I., "Preconditioned URANS Simulation of Synthetic Jet Flows Using Deforming Mesh Method," Ph.D. Dissertation, Department of Aerospace Engineering, Inha Univ., Incheon, ROK, 2011.

[26] Yao, C., Chen, F. J., and Neuhart, D., "Synthetic Jet Flowfield Database for Computational Fluid Dynamic Validation," *AIAA Journal*, Vol. 44, No. 12, 2006, pp. 3153–3157. doi:10.2514/1.13819

[27] Schaeffler, N. W., and Jenkins, L. N., "The Isolated Synthetic Jet in Crossflow: A Benchmark for Flow Control Simulation," AIAA Paper 2004-2219, June 2004.

[28] Schaeffler, N. W., and Jenkins, L. N., "Isolated Synthetic Jet in Crossflow: Experimental Protocols for a Validation Dataset," *AIAA Journal*, Vol. 44, No. 12, 2006, pp. 2846–2856. doi:10.2514/1.13743

[29] Rumsey, C. L., "Computation of a Synthetic Jet in a Turbulent Cross-Flow Boundary Layer," NASA TM-2004-213273, 2004.

[30] Bagheri, V. S., Schlatter, P., Schmid, P. J., and Henningson, D. S., "Global Stability of a Jet in Crossflow," *Journal of Fluid Mechanics*, Vol. 624, No. 9, 2009, pp. 33–44. doi:10.1017/S0022112009006053

[31] Seifert, A., and Pack, L., "Active Flow Separation Control on Wall-Mounted Hump at High Reynolds Numbers," *AIAA Journal*, Vol. 40, No. 7, July 2002, pp. 1363–1372. doi:10.2514/2.1796

[32] Greenblatt, D., Paschal, K. B., Yao, C. S., and Harris, J., "A Separation Control CFD Validation Test Case Part 2. Zero Efflux Oscillatory Blowing," AIAA Paper 2005-0485, Jan. 2005.

[33] Greenblatt, D., Paschal, K. B., Yao, C. S., Harris, J., Schaeffler, N. W., and Washburn, W. E., "A Separation Control CFD Validation Test Case Part 1. Baseline & Steady Suction," AIAA Paper 2004-2220, June 2004.

[34] Rumsey, C. L., "Reynolds-Averaged Navier–Stokes Analysis of Zero Efflux Flow Control over a Hump Model," AIAA Paper 2006-1114, Jan. 2006.

W. Anderson
Associate Editor